computation

MDPI

Article

Operational Robustness of Amino Acid Recognition via Transverse Tunnelling Current Across Metallic Graphene Nano-Ribbon Electrodes: The Pro-Ser Case

Giuseppe Zollo[1,2]

[1] Dipartimento di Scienze di Base e Applicate per l'Ingegneria, Università di Roma "La Sapienza", Via A. Scarpa 14-16, 00161 Rome, Italy; giuseppe.zollo@uniroma1.it

[2] Infrastructure for Energy Transition and Circular Economy @ EuroNanoLab—iENTRANCE@ENL, 00161 Rome, Italy

Abstract: Asymmetric cove-edged graphene nano-ribbons were employed as metallic electrodes in a hybrid gap device structure with zig-zag graphene nano-ribbons terminations for amino acid recognition and peptide sequencing. On a theoretical basis, amino acid recognition is attained by calculating, using the non equilibrium Green function scheme based on density functional theory, the transversal tunnelling current flowing across the gap device during the peptide translocation through the device. The reliability and robustness of this sequencing method versus relevant operations parameters, such as the bias, the gap size, and small perturbations of the atomistic structures, are studied for the paradigmatic case of Pro-Ser model peptide. I evidence that the main features of the tunnelling signal, that allow the recognition, survive for all of the operational conditions explored. I also evidence a sort of geometrical selective sensitivity of the hybrid cove-edged graphene nano-ribbons versus the bias that should be carefully considered for recognition.

Keywords: non equilibrium green function; first principles; edge engineered graphene nano-ribbons; tunnelling current; amino acid recognition; peptide sequencing

Academic Editor: Aleksey E. Kuznetsov

Received: 16 December 2024
Revised: 8 January 2025
Accepted: 15 January 2025
Published: 21 January 2025

Citation: Zollo, G. Operational Robustness of Amino Acid Recognition via Transverse Tunnelling Current Across Metallic Graphene Nano-Ribbon Electrodes: The Pro-Ser Case. *Computation* **2025**, *13*, 22. https://doi.org/10.3390/computation13020022

1. Introduction

Efficient single-residue sequencing techniques of the primary structure of proteins are of fundamental importance for proteomics to detect mutations or post-translational modifications that are the cause of illnesses. Indeed, present state-of-the-art sequencing methods are limited, as they exploit time consuming and expensive processes such as protein degradation into small peptides and their recognition via mass spectroscopy and data processing from protein data banks.

Therefore, new sequencing methods and devices at the nanoscale are being considered for biomolecules and proteins [1–12].

Among them, two main methods exploiting different sensing observables are worth to be mentioned: the blockage of the ionic current and the transversal tunnelling current. The first one is measured along a nano-pore axis during the peptide translocation [5–10,12,13]; hence the single AA recognition is inhibited as the axial ionic current contains information from several residues of the protein [14].

The transversal tunnelling current, instead, flows across two nano-electrodes while the protein translocates through a solid-state nano-gap [15] and benefits from the quantum mechanical nature of the signal which must reflect the atomistic-scale properties of the

residue that is in the middle of the nano-gap at a given time [11,16,17]. In the last category, proposals can be found for either tailored or unbiased recognition.

To perform sequencing at the nanoscale with both the above methods, the translocation dynamics of the protein must be controlled, and this remains a challenge. However, the second method would allow, at least in principle, the atomistic scale AAs recognition if 2D or 1D electrodes were employed.

Hence, graphene based devices have been considered as a natural choice to this aim [4,18–26].

In the last few years, some articles have been published proposing an ideal device based on sub-nanometer gaps of graphene nano-ribbons (GNR) to sense, at the atomistic scale, single peptide bonds (PB) that might be employed to trigger AA recognition [27–30]. However, the point resolution required to sense the peptide backbone requires the use of narrow graphene nano-ribbon (GNR) electrodes that, besides being technologically challenging, have a semiconducting ground state [31,32]. Therefore, a metallic metastable state was employed, as the non equilibrium Green functions approach (NEGF) based on the density functional theory (DFT) scheme assumes metallic electrodes. This choice was supported by the discover that metallicity could be induced in graphene nano-ribbons by doping [33] or in static transversal electric field [34]. More interestingly, recent findings have shown that edge engineering through bottom-up strategies, such as cove-edged and zero-mode superlattice, can be employed to obtain metallic zig-zag nano-ribbons [35,36].

Hence, using such a narrow GNR, the problem of sensing the peptide backbone was approached on a theoretical basis in the context NEGF-DFT and the Landauer–Büttiker formula [37–40], focussing on some small model peptides with neutral and polar residues, such as Gly and Ala homo-peptides, Gly-Ala, Gly-Asn, neutral Gly-Asp, and polar Asn homo-peptides where the important role played by the resonant double bond of the PBs along the GNR direction was evidenced.

More recently, a newly conceived nano-gap, with a hybrid GNR structure and 1D asymmetric cove-edged GNR, real metallic, electrodes, has been employed showing that the main findings already reported for the simple Gly homo-peptide still hold [41]. Being inspired by these works, in the present article, I focus on the Pro-Ser case to study the dependence of the tunnelling signal on some fundamental physical quantities that are supposed to affect the recognition in a real device, namely the bias between the electrodes and the nano-gap size. This case study is particularly interesting because it involves the recognition of proline, which is interesting for its antimicrobial and cell-penetrating activities [42,43], but also from the structural point of view because of its unique "closed" side chain that increases the rigidity of the proteins primary structure. For the present case I also study the dependence of the tunnelling current on a modelling parameter that might affect the prediction, i.e., the relaxation threshold of the quantum mechanical stage (see below the simulation protocol), which affects the actual atomistic configurations considered.

2. Computational Methods

The gap nano-structure employed is a hybrid structure with two unit cells of asymmetric cove-edged zig-zag GNR (ZGNR) (8 C rows each), which will be indicated in the following as Asymmetric Cove Edged Zig-Zag Graphene Nano-Ribbons (8AsCEZGNR) [35] (the width is $d_w \approx 1.6$ nm including the hydrogens), each of them joined to one terminal piece of zig-zag GNRs with 6 carbon rows (6ZGNR). The electrodes are two semi-infinite 8AsCEZGNR attached to the terminal of the device. The scheme is drawn in Figure 1. This structure has been studied in the context of DFT, and the following main statements were established: the 8AsCEZGNRs are metallic (see below) and, therefore, can be used as metallic electrodes, as one would normally perform with gold electrodes, but taking

the remarkable advantages of using a carbon based 1D structure, which allows an ideal atomistic resolution of the nano-device, and also exploiting the exceptional control of the carbon technology at the nano-scale. Moreover, I have previously studied the properties of the hybrid 8AsCEZGNR−6ZGNR device showing that it retains the metallic nature of the external asymmetric cove edged 8AsCEZGNR pieces, and that spin polarised and spin unpolarised models are degenerate [41]. Hence, a spin unpolarised model, in particular the Perdew–Burke–Ernzerhof (PBE) [44] functional is used for the electron exchange and correlation potential $V_{xc}[n(\mathbf{r})]$ because it guarantees a better accuracy than LDA. The nano-gap device has been fully relaxed in the context of DFT using split-double-ζ basis set augmented with polarisation orbitals (DZP), using a mesh cutoff of 300 Ry. Norm-conserving pseudopotentials built with the Troullier–Martins scheme [45] and PBE functional are employed.To this purpose, the SIESTA package (v4.1.5) [46] has been employed.

The gap between the two pieces of ZGNRs has been varied from $d_G = 5$ Å to $d_G = 7$ Å, with increasing steps of $\Delta d_G = 0.5$ Å [27–30,41] and the peptide is pulled across the gap simulating a translocation dynamics. The device axis is oriented along the y-direction, the peptide is translocated along the x-axis and the hydrogenated gap edges are along the z-axis. The narrow gap sizes here employed, that are challenging but close to the present capabilities of nano-technology [3], constrains the translocating residues in almost repeatable and controlled configurations.

Our test case is the Pro-Ser model peptide: it contains 12 amino acids (6 Pro and 6 Ser residues). The peptide has been translocated across the gap in water ambient by non-equilibrium steered classical molecular dynamics (SMD), as implemented in LAMMPS [47], and some configurations have been selected and further processed, as detailed below. Before performing the SMD, five preliminary stages have been performed to prepare the system: a first minimisation stage of the peptide in water, followed by two NVT ($T = 300$ K) stages in bulk water, where the second one aimed to keep the peptide elongated by applying weak forces at the C- and N-terminals. Then, two NPT ($T = 300$ K, $P = 1$ atm) equilibration stages have been performed: the first one to equilibrate at $P = 1$ atm the peptide water system, and the second one to equilibrate, at the same thermodynamic conditions, the system with the nano-gap slit inserted. Finally, I perform the SMD at constant velocity ($v = 10^{-4}$ Å/fs, $k = 5$ kcal/(mol Å^2)) and $T = 300$ K by applying a pulling force at the C-terminal of the peptide. The applied thermostat and barostats are based on a Nosé–Hoover approach, according to Shinoda equations [48], as implemented in LAMMPS. The simulation time of the SMD stage is in the range 8 ns $\leq t_{SMD} \leq$ 9 ns so that for each case I have collected at least 13 passages of the entire peptide across the gap, exploiting the periodic boundary conditions (PBC) along the translocation direction. For all of the classical MD and SMD stages, I have employed the CHARMM force field for the peptides and waters (TIP3P) and the AIREBO [49] model potential for the hydrogenated graphene slit.

Among all of the translocation configurations collected, 13 translocations of 6 identical copies of Pro-Ser pairs (78 configurations), I have selected the one with the minimum strain with respect to the peptide in equilibrium at rest. The reason why I consider this as the most reliable starting point for the next stage is because the constant velocity value employed in the SMD is much larger than the typical velocities of the experimental translocations, implying a larger strain in the simulation, that is basically artificial and that must be cured in the following steps. Moreover, the DFT relaxation stage is also necessary to consider the "real" forces exchanged by the peptides and the solid state device, that in the classical SMD steps is modelled with classical potentials. In particular, I have selected groups of four consecutive residues with the smallest strain, then I have enlarged the selection to 6 residues and, given this piece of peptide, properly terminated, for further relaxation in the DFT

context as detailed below. The selected configurations have, indeed, been further relaxed at $T = 0$ K, in the context of GGA-PBE density functional theory [44], using the same computational parameters detailed previously. The atomic force threshold of the structural relaxation should be chosen to perform a "mild" relaxation to reduce the artificial strain and, at the same time, maintain some residual thermal disorder of the SMD configurations. However, this qualitative requirement should be quantified with an appropriate choice of the atomic forces threshold that controls the degree of the atomistic optimisation on the DFT relaxation stage. As a consequence, this choice might affect the tunnelling current. For this reason, in this article it is addressed the behaviour of the tunnelling current for differently relaxed configurations that are attained with different force threshold values, ranging from $f_{thr} = 1$ eV/Å, which is the largest one here considered, down to $f_{thr} = 0.2$ eV/Å. The last value is two times larger than the default value $f_{thr} = 0.1$ eV/Å of SIESTA. The maximum RMSD per atom measured between the quantum relaxed and the SMD configurations is approximately 3×10^{-2} Å/atom for $f_{thr} = 0.2$ eV/Å. The DFT-based stages, namely the quantum partial relaxation and the transport calculations, have been carried out in dry ambient, without water molecules, since the presence of water does not affect the transport properties of the ZGNR nano-gap because of the hydrophobic character of graphene [27,29,50]. According to the relevant literature, and up to the author's knowledge, the experimental evidences of modified graphene conductivity are most probably due to oxygen containing groups at the GNR edges [51], a marked different situation with respect to the present hydrogenated GNRs. Lastly, the gap sizes considered here prevent the passage at the same time of the peptide chain and of water molecules. In any case, the signature of the water molecules, that might be eventually present in the gap, can be easily filtered because it is one order of magnitude smaller than the ones for the peptide [27,29].

After the relaxation, I have calculated the transmission function and the tunnelling current according to the DFT-NEGF scheme [38], as implemented in the TRANSIESTA code [39]: although it is a ground-state theory, and not a steady-state one, DFT-NEGF is the most popular approach for steady-state transport in nano-structures, and has been successfully applied in many cases with results similar to the ones obtained with formally correct steady stated methods [52,53]. According to DFT-NEGF, the transmission function is

$$T_\sigma(\varepsilon) = \mathrm{Tr}\Big[G(\varepsilon)\Gamma_L(\varepsilon)G^\dagger(\varepsilon)\Gamma_R(\varepsilon)\Big] \tag{1}$$

where $G(\varepsilon) = \lim_{\eta\to 0^+}(\varepsilon + i\eta - H)^{-1}$ is the Green's function of the system, and $\Gamma_{L(R)}(\varepsilon) = i[\Sigma_{L(R)}(\varepsilon) - \Sigma^\dagger_{L(R)}(\varepsilon)]$ is the left (right) coupling function, and $\Sigma_{L(R)}$ is the left (right) electrode self energy [38], which accounts for the renormalisation of the electrons energy in the device region due to the presence of the electrodes. The related tunnelling current is obtained through the Landauer–Büttiker formula [37] for an external bias voltage $V = 1$ V applied along the z direction

$$I(V) = \frac{e}{h}\int_{-\infty}^{+\infty} d\varepsilon\; T(\varepsilon, V) \times [f(\varepsilon - \mu_L) - f(\varepsilon - \mu_R)] \tag{2}$$

where $f(\varepsilon)$ is the Fermi–Dirac distribution function, and $\mu_{L(R)}$ is the electrochemical potential of the left (right) electrode.

Let us now discuss the sampling scheme I have adopted to retrieve the tunnelling current curves. I remind that, after the SMD stage, I have selected a piece with six residues of the original peptide and containing in the middle four peptides with the smallest strain. Then, I have focussed on the two central residues (the central Pro-Ser pair, namely Pro_3-Ser_4) and on their relevant chemical groups that characterise the peptide chain: these chemical groups are the carboxyl CO and the amino NH groups (which are involved in the formation

of the peptide bonds), the $C_\alpha H$ group of the backbone chain and, finally, the side chain SC chain that is attached to the $C_\alpha H$ group. Having these groups in mind, I have defined a sampling grid with the following criteria: each residue is sampled with six configurations having special points right in the middle of the gap during the translocation. The chosen special points are: the bond centre of the amine group (NH), the centre of the bond between the H atom of the amine group and the neighbour C_α atom along the peptide backbone ($CBSN$: centre of bond between the side chain and the N atom), the centre of the bond between the C_α and its H neighbour ($C_\alpha H$), the centre of the bond between the C_α atom and the neighbour C atom of the carboxyl group along the peptide backbone ($CBSC$), the centre of the bond of the carboxyl group (CO), and the centre of the peptide bond PB.

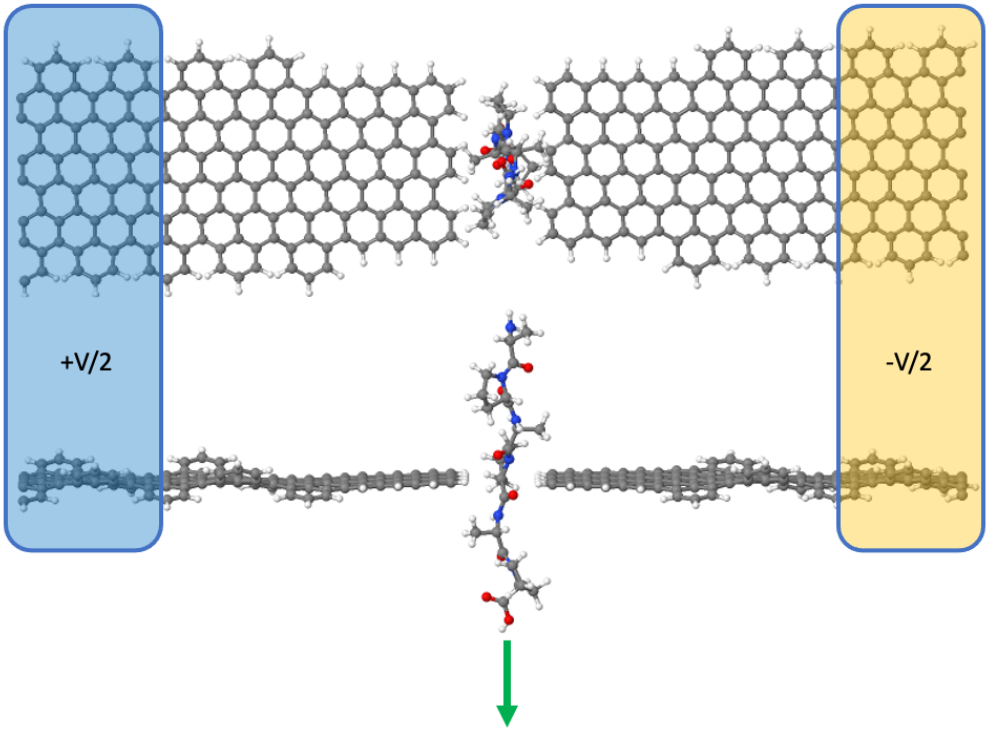

Figure 1. 8AsCEZGNR−6ZGNR nanogap device. Top view (**upper** panel) and side view (**lower** panel). In blue and orange, respectively, the right positive and the left negative electrode regions. In the middle, the device region. The peptide is translocated across the nano-pore (side view) and the tunnelling current flowing across the gap is collected at the electrodes. Carbon, hydrogen, oxygen, and nitrogen atoms are, respectively, grey, white, red, and blue. The green arrow indicates the translocation direction of the peptide.

Then, these special configurations of the two central residues have been relaxed as explained before, with the addition of the peptide bond Ser_2-Pro_3, with a total of 13 relaxed configuration. A denser grid is obtained by rigidly shifting each one of the relaxed configurations one tiny step upward and downward, so that two intermediate sampling points between two relaxed configuration are added. Hence, a sampling grid of 38 points is considered for the selected pair of two consecutive residues, because two consecutive residues are approximately 6.5 Å apart. The grid density is approximately 5.8 samples/Å. Finally, the tunnelling currents have been calculated for all of the relaxed configurations and for the intermediate positions between them.

Because the typical experimental translocation time is in the range [0.1–5.5] ms per amino acid [3], the sampling grid employed here would require a sampling rate of at least 50 kHz in real experiments, which is definitely achievable with the currently available bandwidths of amplifiers and fast pico-ammeters.

The atomistic analysis of the tunnelling current has been provided by studying the atomic current branches between the atoms. They are calculated as [40,54]

$$I^{\sigma}_{n,n'} = e \int d\varepsilon [f_L(\varepsilon) - f_R(\varepsilon)] Tr\left[G_{\sigma}(\varepsilon)\Gamma^{\sigma}{}_{L}(\varepsilon)G^{\dagger}_{\sigma}(\varepsilon)J^{\sigma}_{n,n'}\right] \quad (3)$$

with

$$J^{\sigma}_{n,n'} = \frac{1}{i\hbar}(P_n H_{\sigma} P_{n'} - P_{n'} H_{\sigma} P_n) \quad (4)$$

and the projection operator on the n site $P_n = \sum_{\gamma} |\phi_{n,\gamma}\rangle\langle\phi_{n,\gamma}|$ expressed in terms of a complete localised basis set $\{|\phi_{n,\gamma}\rangle\}$ in a subspace of the full device region where $|\phi_{n,\gamma}\rangle$ is an atomic orbital of type γ, located at the atomic site n [40,54,57].

The detailed electron coupling and transmission across the peptide can be studied by calculating the cumulative atomic bond currents injected from the left lead (electron drain) into the various peptide chemical groups, namely the CO and NH groups involved in the PB, the $C_{\alpha}H$ groups, and the side chains SC, according to [57]

$$I^{\sigma}_{L,G} = \sum_{\alpha,\beta} J^{\sigma}_{\alpha,\beta} \quad \alpha \in L \quad \beta \in G \quad (5)$$

where L is the left lead and G is one of the previous groups that can be employed to ideally decompose the peptide. The bond currents are calculated using the sisl package (v1.14.3) [57].

3. Results and Discussion

I first analyse the dependence of the tunnelling current of the Pro-Ser model peptide translocation configurations on the maximum value of the residual force allowed (force relaxation threshold) that are shown in Figure 2. Let's consider the Pro-Ser signal for the lowest threshold $f_{thr} = 0.2$ eV/Å. The signal (black line) is characterised by a high peak in the "Pro" region between N_{Pro} and $CBSC_{Pro}$, a small peak, in the "Ser" region between N_{Ser} and $CBSC_{Ser}$, approximately located at $CBSN_{Ser}$, a double peak structure around the Ser-Pro peptide bond (region between CO_{Ser} and N_{Pro}), and finally a region around the Pro-Ser peptide bond with no meaningful signal. The large peak at $C_{\alpha}H_{Pro}$ is due to the tunnelling across the in-plane Pro platelet, the small signal at $CBSN_{Ser}$ is caused by the tunnelling across the Ser side chain, which is poor for hydrophobic alkyl groups, and finally the structure around the Ser−Pro peptide is due to the tunnelling across the out of gap plane Pro Platelet that, however, is close enough to the gap plane.

As one can see, the main features described above for the relaxed configuration with $f_{thr} = 0.2$ eV/Å force threshold are still present for all of the other configurations obtained with larger force thresholds. I have not reported the case with $f_{thr} = 0.6$ eV/Å that, practically, is superimposed to the curve obtained for relaxed configurations with $f_{thr} = 0.4$ eV/Å. As a general observation, it can be stated that, with a force threshold greater than $f_{thr} = 0.4$ eV/Å, the curves are quite similar (they can be considered equivalent), but some interesting different details, that are of secondary importance, emerge with respect to the curve obtained with a relaxation threshold $f_{thr} = 0.2$ eV/Å. These details concern a small secondary peak, visible for the configurations relaxed with $f_{thr} \geq 0.4$ eV/Å, close to $C_{\alpha}H_{Ser}$, which disappears for the relaxation threshold at $f_{thr} = 0.2$ eV/Å, a certain difference of the peak intensities in the Ser-Pro peptide bond region and, finally, the small feature, visible at NH_{Ser} for $f_{thr} = 0.2$ eV/Å, but not for greater threshold values. The atomic groups current analysis reveals that the secondary feature of the current signal at

$C_\alpha H_{Ser}$ is due to a better alignment of the neighbouring Pro platelet that contributes to the tunnelling, as detailed in Figure 3.

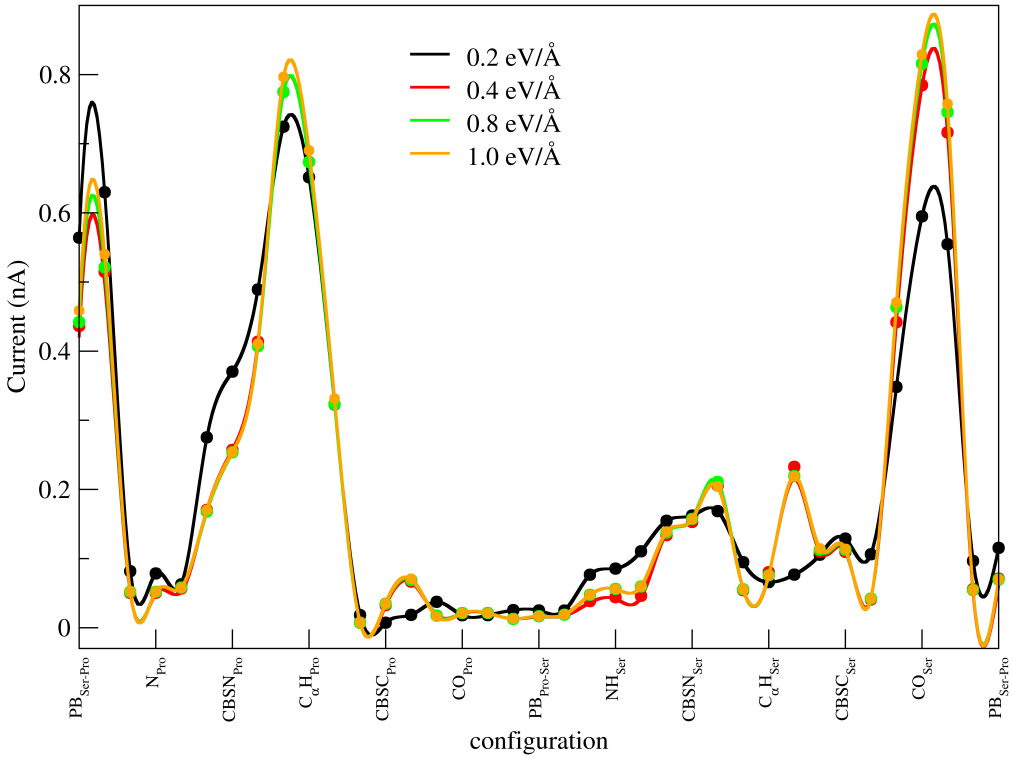

Figure 2. Pro-Ser tunnelling currents obtained for relaxed configurations with different force threshold values.

Looking at the general behaviour, it can be stated that the relaxation stage is not very critical in the explored range. Some minor difference only emerges with the lowest employed force threshold while the signal appears virtually insensitive to the force threshold in the range (1.0 eV/Å $\leq f_{thr} \leq$ 0.4 eV/Å). As mentioned, this stage would not be necessary in case the theoretical translocation was performed in an ab initio (or QM/MM) context with, however, much heavier computational workload that would not allow a systematic study for different cases. Strictly speaking, the limited sensitivity of the tunnelling current on the relaxation threshold regards the robustness of the multi-scale computational protocol adopted, showing that a higher of lower degree of strain and "thermal" disorder surviving after the DFT partial optimisation stage does not affect the recognition. This aspect might indicate that the constraint of the narrow gap somehow makes the translocation configurations of a given pair of AAs close enough to each other to ensure reproducibility and recognition. However, this must be checked by analysing different translocation configurations other then the one with the minimal strain considered here. The eventual experimental recognition should benefit from the constraint that the narrow nanogap employed exerts on the residues in the gap, although this would make more challenging both the device manufacturing and the translocation process.

I now analyse the dependence of the Pro-Ser tunnelling signal versus the bias. I have calculated the signal for bias values in the range (0.1 V $\leq V_{bias} \leq$ 1.0 V) with increasing steps of $V_{bias} = 0.1$ V), for configurations relaxed with a force threshold $f_{thr} =$ 0.2 eV/Å and gap-size $d_{gap} = 5$ Å. The signals are reported in Figure 4.

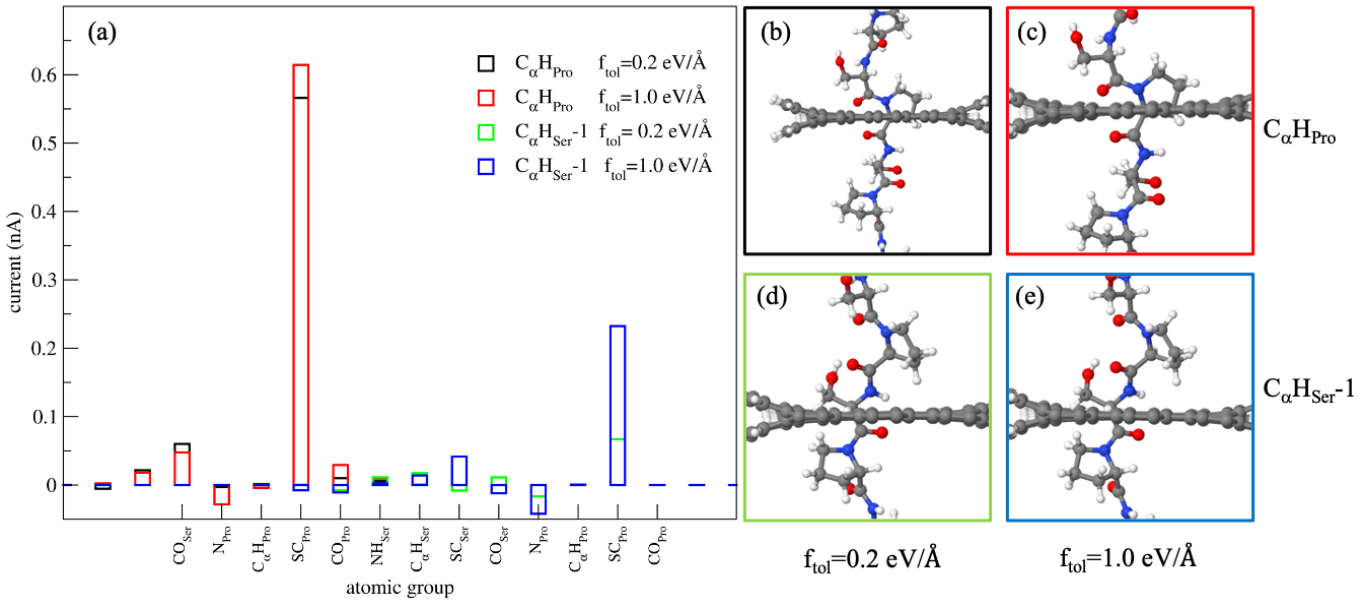

Figure 3. Grouped bond currents for two relevant configurations, namely $C_\alpha H_{Ser} - 1$ and $C_\alpha H_{Pro}$, relaxed with a force threshold of $f_{thr} = 0.2$ eV/Å and $f_{thr} = 0.2$ eV/Å (**a**). I report the corresponding atomistic configurations for $f_{thr} = 0.2$ eV/Å (**b**,**d**) and for $f_{thr} = 1.0$ eV/Å (**c**,**e**).

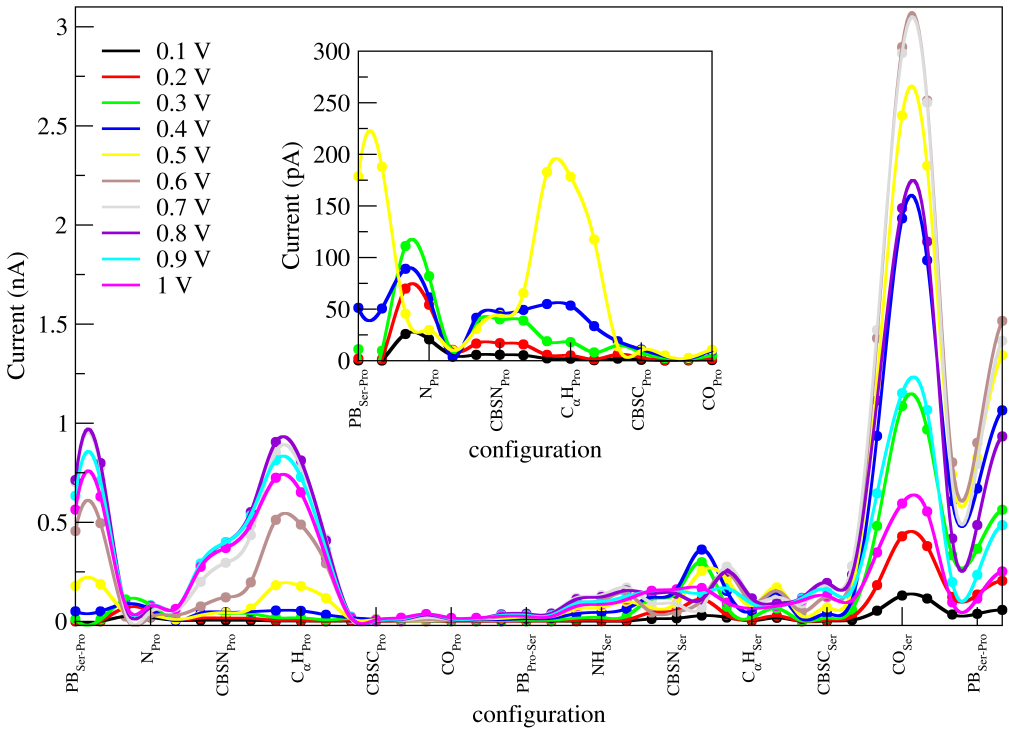

Figure 4. Tunnelling current of Pro-Ser for gap size $d_{gap} = 5$ Å, force threshold tolerance $f_{tol} = 0.2$ eV/Å, and with variable bias in the range (0.1 V $\leq V_{bias} \leq$ 1.0 V). In the inset is shown a magnified view of the Pro signal for bias values (0.1 V $\leq V_{bias} \leq$ 0.5 V) to better evidence its rise with the bias.

It is shown that the signal has different behaviours with the bias: the Pro signal, caused by the tunnelling current across the hydrophobic part of the Pro platelet at the $C_\alpha H_{Pro}$ configuration, is very low for low bias, rises with the bias, with a maximum at $V_{bias} = 0.8$ V, and then reduces a little at $V_{bias} = 1.0$ V. For low bias values, the Pro signal (i.e., the tunnelling signal flowing across the Pro platelet) is somehow anticipated at N_{Pro}, and has

the order of magnitude of tens of ps. The peak at CO_{Ser} has a maximum at $V_{bias} = 0.6$ V, and is then reduced down to less than half of the maximum at $V_{bias} = 0.6$ V. A small peak at $CBSN_{Ser} - 1$ obtains its maximum at $V_{bias} = 0.4$ V. To better evidence this behaviour, I show the maxima of the two peaks versus the bias in Figure 5.

Once again, to understand this behaviour I apply the bond current analysis for the three peaks reported in Figure 5 at different bias values, namely the bias at the maxima shown Figure 5 and at $V_{bias} =$ 1.0 V, as reported in Figure 6.

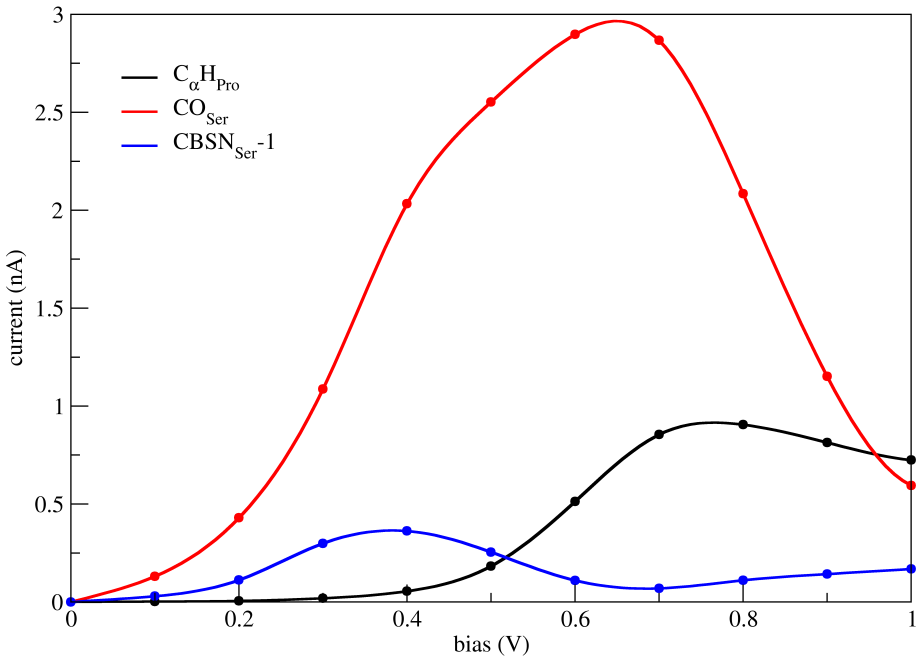

Figure 5. Behaviour of the tunnelling current main peaks versus the bias in the range (0.1 V $\leq V_{bias} \leq$ 1.0 V) for the Pro-Ser model peptide with gap size $d_{gap} =$ 5Å, force threshold tolerance $f_{tol} =$ 0.2 eV/Å.

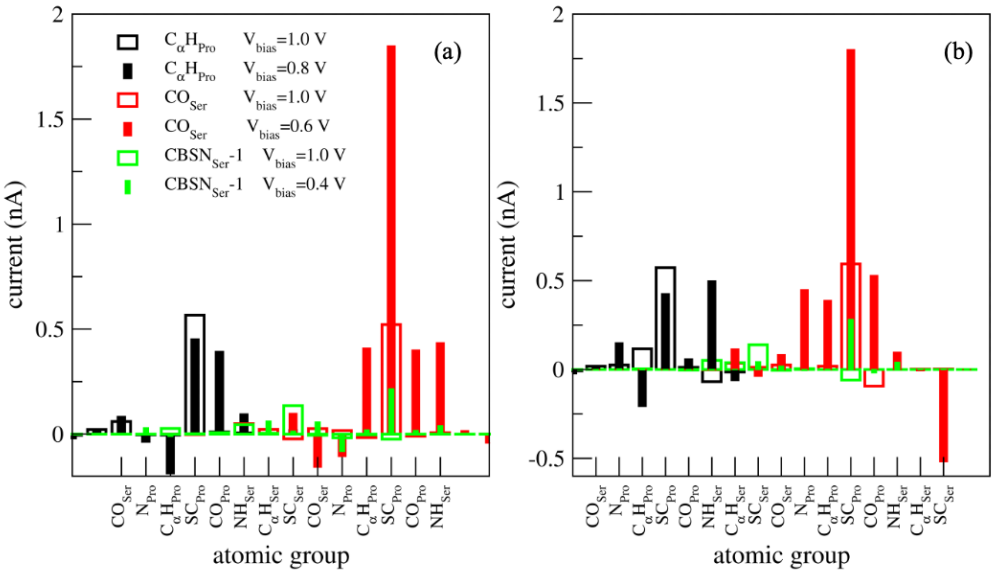

Figure 6. Grouped bond currents of the Pro-Ser current main peaks. Current is injected from the positive left electrode (**a**) and collected into the right negative electrode (**b**). The grouped bond currents are calculated for the reference bias of $V_{bias} = 1$ V and for the bias values corresponding to the maximum of the three main peaks, as shown in Figure 5. The gap size is $d_{gap} =$ 5 Å, and the force threshold tolerance $f_{tol} =$ 0.2 eV/Å.

For $CBSN_{Ser} - 1$, an unexpected contribution from the Pro residue at $V_{bias} = 0.4$ V is noticed, which is the lower neighbour of Ser. A deeper analysis of the contributions of the main groups, namely the Ser and the lower neighbour Pro side-chains, versus the bias is shown in Figure 7. It is shown that for low bias the, "Ser" signal is supplied by the tunnelling across the lower Pro side-chain, while the real sensing of the pro Side chain is obtained for bias values in the range (0.6 V$\leq V_{bias} \leq$ 1.0 V); hence, it can be observed a sort of "tuning" effect of the bias showing that the device can sense different pieces of the neighbouring atomic structure, depending on the bias. As shown in the inset, in the $CBSN_{Ser} - 1$ configurations, the hydrophobic parts of the Ser and Pro side chains are close to the sensing plane, and in opposite directions, so that, in the present case, the bias can switch the sensing to the left or to the right side of the gap, indicating that the behaviour of the sensing device is more complex than expected as the transmission channel might change with the bias. This is not the case for the $C_{\alpha}H_{Pro}$ and CO_{Ser} peaks that show a well define maximum in the bias range. for $CBSN_{Ser} - 1$; instead, the presence of a relative minimum at $V_{bias} \approx 0.7$ V is a strong indication of a transmission channel change at this bias value.

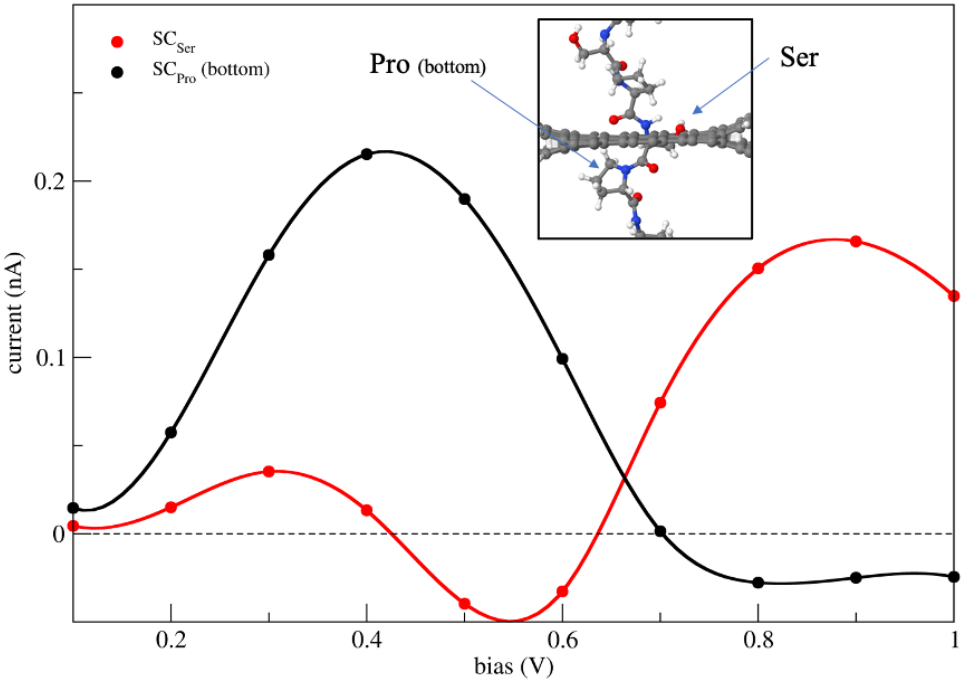

Figure 7. SC_{Ser} and SC_{Pro} contributions to the $CBSN_{Ser} - 1$ peak versus the bias. In the inset is shown the $CBSN_{Ser} - 1$ configuration, where the arrows indicate the side chains through which the tunnelling current flows.

This aspect is better understood projecting the transmission function on the device eigenstates and by calculating the eigenchannels, i.e., the unitary combination of incoming states $|\Phi_l\rangle = \sum_{l'} U_{l,l'}|\Psi_{l'}\rangle$ that makes the transmission matrix diagonal at a given energy $T_e = diag(T_1, T_2 \dots)$ [58]. The transmissions have been projected on the right and left hybrid nano-ribbons in the device region, having in mind that the incoming electrons proceed from the right to the left. The projected transmissions and eigenstates calculated at the energy where the transmission is maximum are shown in Figures 8 and 9 for a bias of $V_{bias} = 1$ V and $V_{bias} = 0.4$ V, respectively.

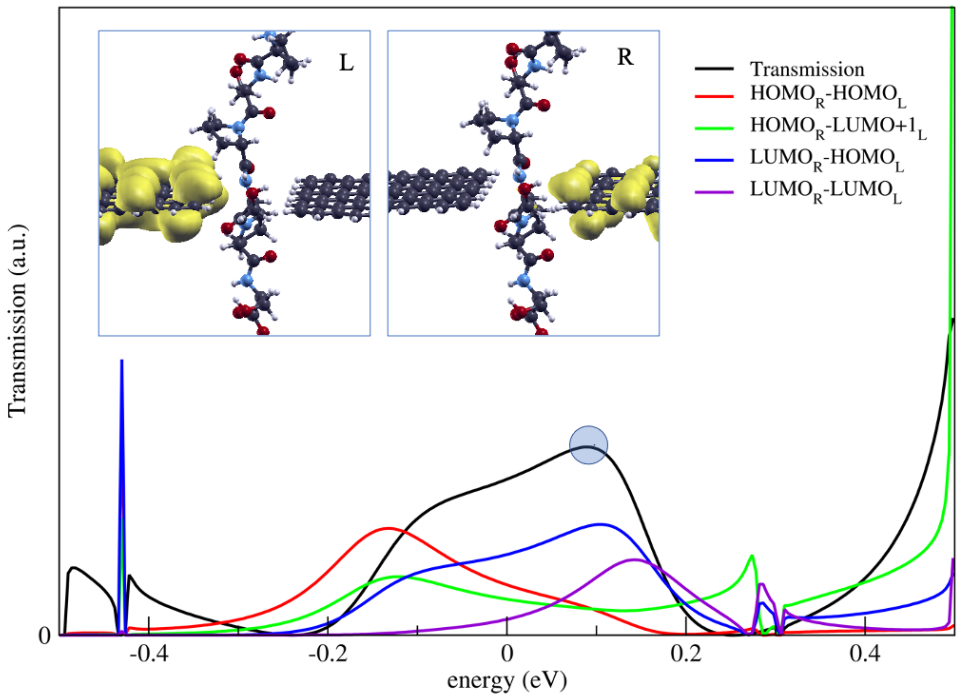

Figure 8. Projections of the transmission amplitude between molecular orbitals of the right (incoming electrons) and the left hybrid nano-ribbons in the device region for $CBSN_{Ser} - 1$ at $V_{bias} = 1$ V and the $CBSN_{Ser} - 1$. In the inset are shown the left and right eigenchannels at $E = 0.09$ eV, where the transmission has a maximum.

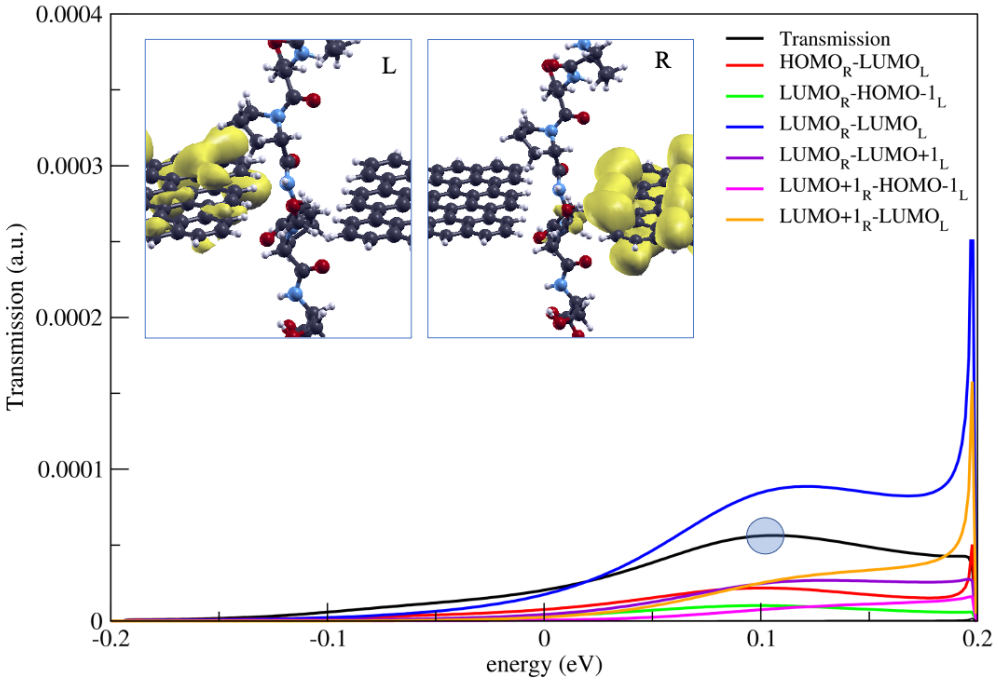

Figure 9. Projections of the transmission amplitude between molecular orbitals of the right (incoming electrons) and the left hybrid nano-ribbons in the device region for $CBSN_{Ser} - 1$ at $V_{bias} = 0.4$ V. In the insets are shown the left and right eigenchannels at $E = 0.106$ eV, where the transmission has a maximum.

For $V_{bias} = 1$ V the major contributions to the transmission come from the reported projections, especially $LUMO_R \rightarrow HOMO_L$, and the resulting eigenchannel is almost uniform at both sides, with a slightly larger density at the Ser side of the $CBSN_{Ser} - 1$

configuration, thus indicating that the Ser side chain is sensed. For $V_{bias} = 0.4$ V, the scenario appears to be more complicated, with more projections contributing to the transmission especially the ones involving LUMO and LUMO + 1 at both the sides of the nanogap. In this case, however, the resulting eigenchannel is markedly not uniform at the left side, with a larger density at the "Pro" side, i.e., close to the lower proline residue of the $CBSN_{Ser} - 1$ configuration, thus indicating that the lower Pro side chain is sensed.

Finally, I consider the tunnelling current of the Pro-Ser model peptide calculated with different gap sizes in the range (5 Å $\leq d_{gap} \leq 7$ Å). The employed bias and force threshold are, respectively $V_{bias} = 1$ V and $f_{thr} = 0.2$ eV/Å. Because the tunnelling currents differ by orders of magnitude for the different gap sizes, I plot them in a logarithmic scale, as shown in Figure 10.

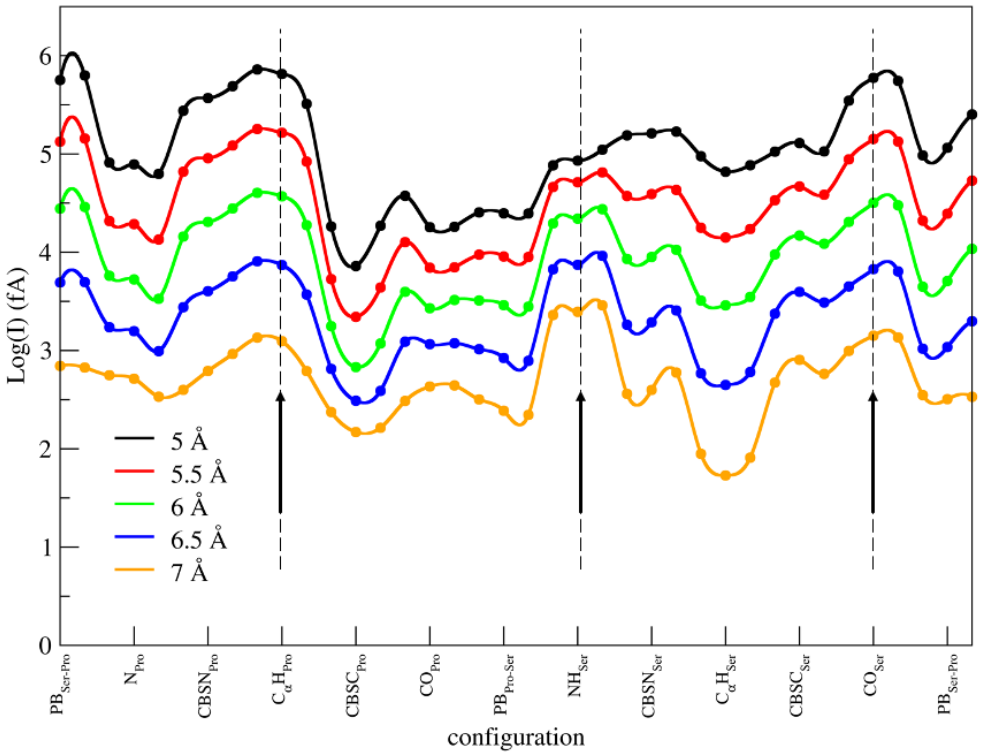

Figure 10. Pro-Ser tunnelling current for different gap sizes. The tunnelling current is in fA, and the current is reported in logarithmic scale. The adopted force threshold and bias are, respectively, $f_{thr} = 0.2$ eV/Å and $V_{bias} = 1$ V.

First of all, it can be noticed that the tunnelling current drops from the nA order of magnitude with $d_{gap} = 5$ Å down to the pA order of magnitude with $d_{gap} = 7$ Å. Hence, even with the largest gap size examined the tunnelling signal is still within the measurable range of the current pico-ammeters. The three main peaks that characterise the Pro-Ser signal are still visible for all of the explored gap sizes (and are indicated by the arrows in Figure 10), but the signal attributed to the Ser residue survives at the NH_{Ser} configuration, instead of the already examined $CBSN_{Ser} - 1$ one that is, however, very close. The grouped bond current analysis shows that the tunnelling still flows across the Pro and Ser side chains for the configurations corresponding to the main peaks of the Pro and Ser residues, even for the largest gap size employed $d_{gap} = 7$ Å (see Figure 11), with the current peaks of the order of pA. If one compares the grouped bond currents reported here with the ones obtained for $d_{gap} = 5$ Å it can be seen that the reduction in the tunnelling is less than three orders of magnitude, from approximately 0.6 nA to 1 pA for the $C_{\alpha}H_{Pro}$, as reported in Figure 3a (see the contribution from SC_{Pro}).

A similar conclusion was obtained using the narrow idealised template electrodes of a simple 2GNR (two rows GNRs) in their metallic metastable phase, employed to sense the peptide backbone and the peptide bonds related signals. This time, however, it can be found a similar scaling law with "real" metallic electrodes that are wide enough to sense the residues and allow for the amino acid recognition.

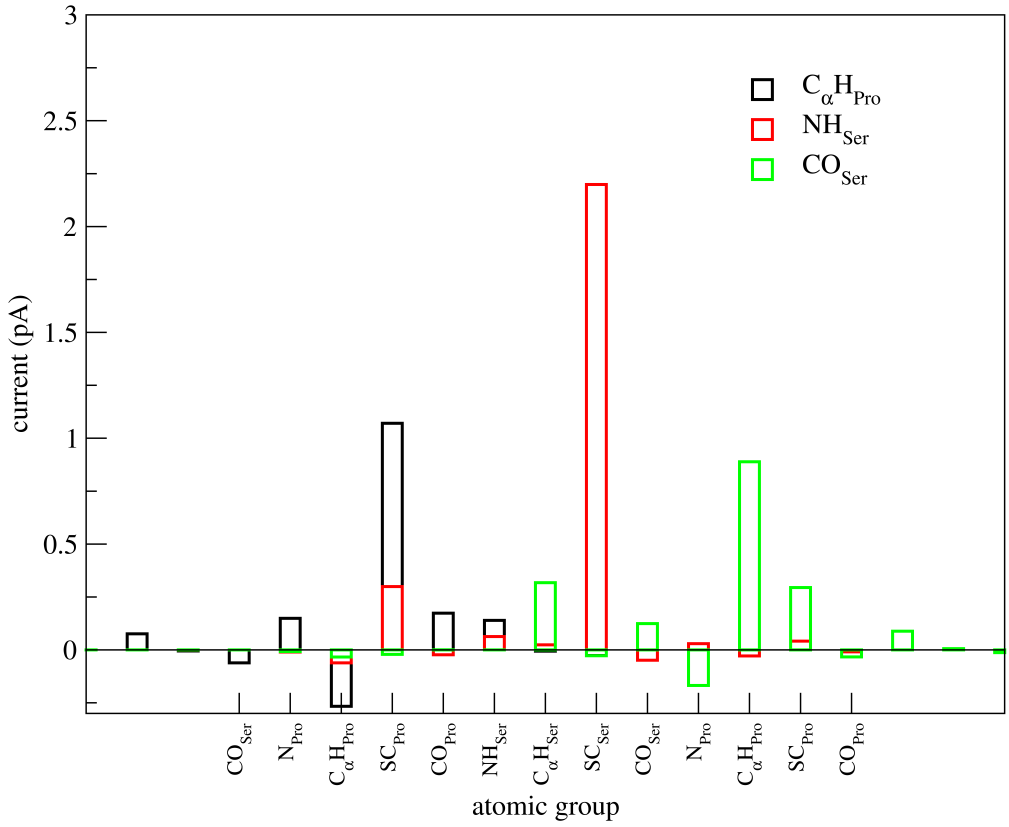

Figure 11. Grouped bond current analysis injected from the right positive lead into the peptide for the $C_\alpha H_{Pro}$ and NH_{Ser} configurations with a gap size of $d_{gap} = 7$ Å and $V_{bias} = 1$ V, $f_{tol} = 0.2$ eV/Å.

The three aspects covered in this section, i.e., the signal change with the threshold of the DFT relaxation stage (that is peculiar of the adopted multi-scale simulation protocol), the bias and, finally, the gap size, although being evaluated for a single special case, namely Pro-Ser, have evidenced that the adopted recognition protocol is robust. The same kind of paradigm, with narrower electrodes, has been applied for sensing a triggering signal from the backbone of model peptides, and has been revealed as rather general. In the present case, where recognition, not triggering, is addressed, reliability, repeatability and robustness are crucial aspects. The adopted protocol might easily be extended to generic sequences of amino acids, provided the main tunnelling signal features of the AAs are properly categorised.

4. Conclusions

I conclude by emphasising the main findings reported and discussed in the present study. I have examined the variation in the tunnelling current, which can be collected during the translocation of the Pro-Ser model peptide, with the bias, the gap size and the atomic positions of the partially relaxed reference configurations for a sensing nano-gap device made of asymmetric cove edged GNR metallic electrodes. The gap size and the bias are two critical operating parameters of an eventual real sensing experiment using the proposed nano-device. The last aspect, on the contrary, addresses a computational

issue related to the employed computational protocol that uses classical SMD to select the translocation configurations and DFT-NEGF to calculate the tunnelling current. The reported results for this last issue are, fortunately, comforting, because it is seen that the variation in the tunnelling signal with the relaxation force threshold is somehow limited, and all of the main features of the signal are retained for all of the relaxation thresholds explored. This make us confident that the thermal fluctuations of the signal might possibly not affect the recognition. A more complex behaviour of the tunnelling current with the bias is found. Even for the lowest bias $V_{bias} = 0.1$ V, I obtain a measurable signal of the order of tens of *ps*, which is still characterised by clear features related to the Pro and Ser side chains. The overall behaviour of the signal versus the bias shows that the main peaks are generally maximised at bias values lower than the maximum. The analysis of the grouped bond currents indicate that in case the peak has only one, well-defined, maximum versus the bias, then the transmission channel is preserved for all of the bias values. On the contrary there might be cases where the current shows also a relative minimum at a given bias. In that case, I have found that the transmission channel might change with the bias. Therefore, a better characterisation of the device behaviour versus the bias is required. Finally, I have analysed the signal for increasing gap sizes, showing that it is reduced by a little more than one order of magnitude per Å, but still remains within the measurable range of state-of-the-art pico-ammeters. The present results unveil some (still uncovered) aspects of non-selective amino acid recognition at the atomic scale by a transversal tunnelling current, thus making a step forward, toward the experimental realisation of the proposed device.

Funding: This research was partially founded by the European Union, Next Generation EU, Mission 4, Component 2, CUP B33C22000710006, Project iENTRANCE@ENL-INFRASTRUCTURE FOR ENERGY TRANSITION AND CIRCULAR ECONOMY@ EURO NANOLAB.

Data Availability Statement: Data for this article, including selected and relaxed configurations of of Pro containing peptides are available at Open Science Framework at URL: https://osf.io/nr9ut (accessed on 15 January 2025).

Acknowledgments: We acknowledge PRACE for awarding access to the Fenix Infrastructure resources at CINECA-ITALY, which are partially funded from the European Union's Horizon 2020 research and innovation programme through the ICEI project under the grant agreement No. 800858. I acknowledge CRESCO/ENEAGRID High Performance Computing infrastructure and its staff [57] for providing additional computational support. CRESCO/ENEAGRID High Performance Computing infrastructure is funded by ENEA, the Italian National Agency for New Technologies, Energy and Sustainable Economic Development, see https://www.eneagrid.enea.it/CRESCOportal/ (accessed on 15 January 2025) for information.

Conflicts of Interest: The author declares no conflicts of interest.

Abbreviations

The following abbreviations are used in this manuscript:

DFT	Density Functional Theory
NEGF	Non Equilibrium Green Function
SMD	Steered Molecular Dynamics
AA	Amino Acid
ZGNR	Zig-zag Graphene Nano-Ribbon
8AsCEZGNR	8 carbon rows wide Asymmetric Cove Edged ZGNR

References

1. Jain, M.; Fiddes, I.T.; Miga, K.H.; Olsen, H.E.; Paten, B.; Akeson, M. Improved Data Analysis for The MinION Nanopore Sequencer. *Nat. Methods* **2015**, *12*, 351–356. [CrossRef] [PubMed]
2. Schneider, G.F.; Dekker, C. DNA sequencing with nanopores. *Nat. Biotechnol.* **2012**, *30*, 326–328. [CrossRef] [PubMed]
3. Kennedy, E.; Dong, Z.; Tennant, C.; Timp, G. Reading the primary structure of a protein with 0.07 nm^3 resolution using a subnanometre-diameter pore. *Nat. Nanotechnol.* **2016**, *11*, 968–976. [CrossRef]
4. Wilson, J.; Sloman, L.; He, Z.; Aksimentiev, A. Graphene nanopores for protein sequencing. *Adv. Funct. Mater.* **2016**, *26*, 4830–4838. [CrossRef]
5. Di Muccio, G.; Rossini, A.E.; Di Marino, D.; Zollo, G.; Chinappi, M. Insights into protein sequencing with an alpha-Hemolysin nanopore by atomistic simulations. *Sci. Rep.* **2019**, *9*, 6440. [CrossRef] [PubMed]
6. Oukhaled, A.; Bacri, L.; Pastoriza-Gallego, M.; Betton, J.M.; Pelta, J. Sensing proteins through nanopores: Fundamental to applications. *ACS Chem. Biol.* **2012**, *7*, 1935–1949. [CrossRef] [PubMed]
7. Di Marino, D.; Bonome, E.L.; Tramontano, A.; Chinappi, M. All-atom molecular dynamics simulation of protein translocation through an α-hemolysin nanopore. *J. Phys. Chem. Lett.* **2015**, *6*, 2963–2968. [CrossRef]
8. Mereuta, L.; Roy, M.; Asandei, A.; Lee, J.K.; Park, Y.; Andricioaei, I.; Luchian, T. Slowing down single-molecule trafficking through a protein nanopore reveals intermediates for peptide translocation. *Sci. Rep.* **2014**, *4*, 3885. [CrossRef]
9. Tavassoly, O.; Nokhrin, S.; Dmitriev, O.Y.; Lee, J.S. Cu (II) and dopamine bind to α-synuclein and cause large conformational changes. *Febs J.* **2014**, *281*, 2738–2753. [CrossRef] [PubMed]
10. Rodriguez-Larrea, D.; Bayley, H. Multistep protein unfolding during nanopore translocation. *Nat. Nanotechnol.* **2013**, *8*, 288–295. [CrossRef]
11. Ohshiro, T.; Tsutsui, M.; Yokota, K.; Furuhashi, M.; Taniguchi, M.; Kawai, T. Detection of post-translational modifications in single peptides using electron tunnelling currents. *Nat. Nanotechnol.* **2014**, *9*, 835–840. [CrossRef] [PubMed]
12. Rosen, C.B.; Rodriguez-Larrea, D.; Bayley, H. Single-molecule site-specific detection of protein phosphorylation with a nanopore. *Nat. Biotechnol.* **2014**, *32*, 179–181. [CrossRef]
13. Ouldali, H.; Sarthak, K.; Ensslen, T.; Piguet, F.; Manivet, P.; Pelta, J.; Behrends, J.C.; Aksimentiev, A.; Oukhaled, A. Electrical recognition of the twenty proteinogenic amino acids using an aerolysin nanopore. *Nat. Biotechnol.* **2020**, *38*, 176–181. [CrossRef] [PubMed]
14. Asandei, A.; Rossini, A.E.; Chinappi, M.; Park, Y.; Luchian, T. Protein Nanopore-Based Discrimination between Selected Neutral Amino Acids from Polypeptides. *Langmuir* **2017**, *33*, 14451–14459. [CrossRef] [PubMed]
15. Zwolak, M.; Di Ventra, M. Electronic Signature of DNA Nucleotides via Transverse Transport. *Nano Lett.* **2005**, *5*, 421–424. [CrossRef] [PubMed]
16. Di Ventra, M.; Taniguchi, M. Decoding DNA, RNA and peptides with quantum tunnelling. *Nat. Nanotechnol.* **2016**, *11*, 117–126. [CrossRef]
17. Heerema, S.J.; Dekker, C. Graphene nanodevices for DNA sequencing. *Nat. Nanotechnol.* **2016**, *11*, 127–136. [CrossRef]
18. Goyal, G.; Lee, Y.B.; Darvish, A.; Ahn, C.W.; Kim, M.J. Hydrophilic and size-controlled graphene nanopores for protein detection. *Nanotechnology* **2016**, *27*, 495301. [CrossRef] [PubMed]
19. Bonome, E.L.; Lepore, R.; Raimondo, D.; Cecconi, F.; Tramontano, A.; Chinappi, M. Multistep Current Signal in Protein Translocation through Graphene Nanopores. *J. Phys. Chem. B* **2015**, *119*, 5815–5823. [CrossRef] [PubMed]
20. Sarathy, A.; Qiu, H.; Leburton, J.P. Graphene Nanopores for Electronic Recognition of DNA Methylation. *J. Phys. Chem. B* **2017**, *121*, 3757–3763. [CrossRef]
21. Traversi, F.; Raillon, C.; Benameur, S.; Liu, K.; Khlybov, S.; Tosun, M.; Krasnozhon, D.; Kis, A.; Radenovic, A. Detecting the translocation of DNA through a nanopore using graphene nanoribbons. *Nat. Nanotechnol.* **2013**, *8*, 939–945. [CrossRef]
22. Paulechka, E.; Wassenaar, T.A.; Kroenlein, K.; Kazakov, A.; Smolyanitsky, A. Nucleobase-functionalized graphene nanoribbons for accurate high-speed DNA sequencing. *Nanoscale* **2016**, *8*, 1861–1867. [CrossRef] [PubMed]
23. Amorim, R.G.; Rocha, A.R.; Scheicher, R.H. Boosting DNA Recognition Sensitivity of Graphene Nanogaps through Nitrogen Edge Functionalization. *J. Phys. Chem. C* **2016**, *120*, 19384–19388. [CrossRef]
24. Prasongkit, J.; Feliciano, G.T.; Rocha, A.R.; He, Y.; Osotchan, T.; Ahuja, R.; Scheicher, R.H. Theoretical assessment of feasibility to sequence DNA through interlayer electronic tunneling transport at aligned nanopores in bilayer graphene. *Sci. Rep.* **2015**, *5*, 17560. [CrossRef] [PubMed]
25. Postma, H.W.C. Rapid Sequencing of Individual DNA Molecules in Graphene Nanogaps. *Nano Lett.* **2010**, *10*, 420–425. [CrossRef] [PubMed]
26. Prasongkit, J.; Grigoriev, A.; Pathak, B.; Ahuja, R.; Scheicher, R.H. Transverse Conductance of DNA Nucleotides in a Graphene Nanogap from First Principles. *Nano Lett.* **2011**, *11*, 1941–1945. [CrossRef] [PubMed]
27. Rossini, A.E.; Gala, F.; Chinappi, M.; Zollo, G. Peptide bond detection via graphene nanogaps: A proof of principle study. *Nanoscale* **2018**, *10*, 5928–5937. [CrossRef]

28. Civitarese, T.; Zollo, G. Gap Size Dependence of Atomistic-Resolved Peptide Bond Signals by Tunneling Current Across Nano-Gaps of Graphene Nano-Ribbons. *Computation* **2020**, *8*, 29. [CrossRef]
29. Civitarese, T.; Zollo, G. Triggering Amino Acid Detection by Atomistic Resolved Tunneling Current Signals in Graphene Nanoribbon Devices for Peptide Sequencing. *ACS Appl. Nano Mater.* **2021**, *4*, 363–371. [CrossRef]
30. Zollo, G.; Rossini, A.E. Vibration assisted electron tunneling through nano-gaps in graphene nano-ribbons for amino-acid and peptide bond recognition. *Nanoscale Adv.* **2019**, *1*, 3547–3554. [CrossRef]
31. Son, Y.W.; Cohen, M.L.; Louie, S.G. Energy Gaps in Graphene Nanoribbons. *Phys. Rev. Lett.* **2006**, *97*, 216803. [CrossRef] [PubMed]
32. Li, Y.Y.; Chen, M.X.; Weinert, M.; Li, L. Direct experimental determination of onset of electron–electron interactions in gap opening of zigzag graphene nanoribbons. *Nat. Comm.* **2014**, *5*, 4311. [CrossRef] [PubMed]
33. Li, Y.; Zhou, Z.; Shen, P.; Chen, Z. Spin Gapless Semiconductor Metal Half-Metal Properties in Nitrogen-Doped Zigzag Graphene Nanoribbons. *ACS Nano* **2009**, *3*, 1952–1958. [CrossRef] [PubMed]
34. Son, Y.W.; Cohen, M.L.; Louie, S.G. Half-metallic graphene nanoribbons. *Nature* **2006**, *444*, 347–349. [CrossRef] [PubMed]
35. Lee, Y.L.; Zhao, F.; Cao, T.; Ihm, J.; Louie, S.G. Topological Phases in Cove-Edged and Chevron Graphene Nanoribbons: Geometric Structures, Z2 Invariants, and Junction States. *Nano Lett.* **2018**, *18*, 7247–7253. [CrossRef] [PubMed]
36. Rizzo, D.J.; Veber, G.; Jiang, J.; McCurdy, R.; Cao, T.; Bronner, C.; Chen, T.; Louie, S.G.; Fischer, F.R.; Crommie, M.F. Inducing metallicity in graphene nanoribbons via zero-mode superlattices. *Science* **2020**, *369*, 1597–1603. [CrossRef]
37. Stokbro, K.; Taylor, J.; Brandbyge, M.; Mozos, J.L.; Ordejón, P. Theoretical study of the nonlinear conductance of Di-thiol benzene coupled to Au(111) surfaces via thiol and thiolate bonds. *Comput. Mater. Sci.* **2002**, *27*, 151–160. [CrossRef]
38. Datta, S. *Electronic Transport in Mesoscopic Systems*; Cambridge Studies in Semiconductor Physics and Microelectronic Engineering; Cambridge University Press: Cambridge, UK, 1995. [CrossRef]
39. Stokbro, K.; Taylor, J.; Brandbyge, M.; Ordejón, P. TranSIESTA—A Spice for Molecular Electronics. *Ann. N. Y. Acad. Sci.* **2003**, *1006*, 212–226. [CrossRef] [PubMed]
40. Papior, N.; Lorente, N.; Frederiksen, T.; García, A.; Brandbyge, M. Improvements on non-equilibrium and transport Green function techniques: The next-generation transiesta. *Comput. Phys. Commun.* **2017**, *212*, 8–24. [CrossRef]
41. Zollo, G.; Civitarese, T. Ab Initio Properties of Hybrid Cove-Edged Graphene Nanoribbons as Metallic Electrodes for Peptide Sequencing via Transverse Tunneling Current. *ACS Omega* **2022**, *7*, 25164–25170. [CrossRef]
42. Gennaro, R.; Zanetti, M.; Benincasa, M.; Podda, E.; Miani, M. Pro-rich antimicrobial peptides from animals: Structure, biological functions and mechanism of action. *Curr. Pharm. Des.* **2002**, *8*, 763–778. [CrossRef]
43. Pujals, S.; Giralt, E. Proline-rich, amphipathic cell-penetrating peptides. *Adv. Drug Deliv. Rev.* **2008**, *60*, 473–484. [CrossRef]
44. Perdew, J.; Burke, K.; Ernzerhof, M. Generalized Gradient Approximation Made Simple. *Phys. Rev. Lett.* **1996**, *77*, 3865–3868. [CrossRef] [PubMed]
45. Troullier, N.; Martins, J.L. Efficient pseudopotentials for plane-wave calculations. *Phys. Rev. B* **1991**, *43*, 1993–2006. [CrossRef]
46. Soler, J.; Artacho, E.; Gale, J.; García, A.; Junquera, J.; Ordejón, P.; Sánchez-Portal, D. The SIESTA method for ab initio order-N materials simulation. *J. Phys. Condens. Matter* **2002**, *14*, 2745–2779. [CrossRef]
47. Thompson, A.P.; Aktulga, H.M.; Berger, R.; Bolintineanu, D.S.; Brown, W.M.; Crozier, P.S.; in 't Veld, P.J.; Kohlmeyer, A.; Moore, S.G.; Nguyen, T.D.; et al. LAMMPS—A flexible simulation tool for particle-based materials modeling at the atomic, meso, and continuum scales. *Comp. Phys. Comm.* **2022**, *271*, 108171. [CrossRef]
48. Shinoda, W.; Shiga, M.; Mikami, M. Rapid estimation of elastic constants by molecular dynamics simulation under constant stress. *Phys. Rev. B* **2004**, *69*, 134103. [CrossRef]
49. Stuart, S.J.; Tutein, A.B.; Harrison, J.A. A reactive potential for hydrocarbons with intermolecular interactions. *J. Chem. Phys.* **2000**, *112*, 6472–6486. [CrossRef]
50. Feliciano, G.; Sanz-Navarro, C.; Coutinho.Neto, M.; Ordejón, P.; Scheicher, R.H.; Rocha, A.R. Capacitive DNA Detection Driven by Electronic Charge Fluctuations in a Graphene Nanopore. *Phys. Rev. Appl.* **2015**, *3*, 034003. [CrossRef]
51. Yang, Y.; Murali, R. Binding mechanisms of molecular oxygen and moisture to graphene. *Appl. Phys. Lett.* **2011**, *98*, 093116. [CrossRef]
52. Liu, S.; Nurbawono, A.; Zhang, C. Density Functional Theory for Steady-State Nonequilibrium Molecular Junctions. *Sci. Rep.* **2015**, *5*, 15386. [CrossRef] [PubMed]
53. Yam, C.; Zheng, X.; Chen, G.; Wang, Y.; Frauenheim, T.; Niehaus, T.A. Time-dependent versus static quantum transport simulations beyond linear response. *Phys. Rev. B* **2011**, *83*, 245448. [CrossRef]
54. Todorov, T.N. Tight-binding simulation of current-carrying nanostructures. *J. Phys. Condens. Matter* **2002**, *14*, 3049. [CrossRef]
57. Papior, N. sisl: V0.14.3. 2024. Available online: https://zenodo.org/records/14357951 (accessed on 15 January 2025).

58. Paulsson, M.; Brandbyge, M. Transmission eigenchannels from nonequilibrium Green's functions. *Phys. Rev. B* **2007**, *76*, 115117. [CrossRef]
57. Iannone, F.; Ambrosino, F.; Bracco, G.; De Rosa, M.; Funel, A.; Guarnieri, G.; Migliori, S.; Palombi, F.; Ponti, G.; Santomauro, G.; et al. CRESCO ENEA HPC clusters: A working example of a multifabric GPFS Spectrum Scale layout. In Proceedings of the 2019 International Conference on High Performance Computing Simulation (HPCS), Dublin, Ireland, 15–19 July 2019; pp. 1051–1052.